IOP Publishing Phys. Med. Biol. 64 (2019) 235010 (18pp) https://doi.org/10.1088/1361-6560/ab5229

Physics in Medicine & Biology

IPEM Institute of Physics and Engineering in Medicine

PAPER

# Computational analysis of non-invasive deep brain stimulation based on interfering electric fields

RECEIVED
26 January 2019

REVISED
23 September 2019

ACCEPTED FOR PUBLICATION
29 October 2019

PUBLISHED
5 December 2019

Fariba Karimi[1,2], Ahmadreza Attarpour[1,2], Rassoul Amirfattahi[1,3] and Abolghasem Zeidaabadi Nezhad[1]

[1] Department of Electrical and Computer Engineering, Isfahan University of Technology, Isfahan 8415683111, Iran
[2] These authors have contributed equally to this work as first authors.
[3] Author to whom correspondence should be addressed.

**E-mail:** fattahi@cc.iut.ac.ir

**Keywords:** non-invasive deep brain stimulation, temporally interfering electric fields, optimization algorithm, axon modeling

Supplementary material for this article is available online

## Abstract

Neuromodulation modalities are used as effective treatments for some brain disorders. Non-invasive deep brain stimulation (NDBS) via temporally interfering electric fields has emerged recently as a non-invasive strategy for electrically stimulating deep regions in the brain. The objective of this study is to provide insight into the fundamental mechanisms of this strategy and assess the potential uses of this method through computational analysis. Analytical and numerical methods are used to compute the electric potential and field distributions generated during NDBS in homogeneous and inhomogeneous models of the brain. The computational results are used for specifying the activated area in the brain (macroscopic approach), and quantifying its relationships to the stimulation parameters. Two automatic algorithms, using artificial neural network (ANN), are developed for the homogeneous model with two and four electrode pairs to estimate stimulation parameters. Additionally, the extracellular potentials are coupled to the compartmental axon cable model to determine the responses of the neurons to the modulated electric field in two developed models and to evaluate the precise activated area location (microscopic approach). Our results show that although the shape of the activated area was different in macroscopic and microscopic approaches, it located only at depth. Our optimization algorithms showed significant accuracy in estimating stimulation parameters. Moreover, it demonstrated that the more the electrode pairs, the more controllable the activated area. Finally, compartmental axon cable modeling results verified that neurons can demodulate and follow the electric field modulation envelope amplitude (MEA) in our models. The results of this study help develop the NDBS method and eliminate some limitations associated with the nonautomated optimization algorithm.

## 1. Introduction

In the last three decades, non-invasive brain stimulation (NIBS) techniques have shown significant potential to treat some neural diseases (Polanía *et al* 2018). Transcranial direct current stimulation (tDCS) and transcranial magnetic stimulation (TMS) are the most commonly used and safest form of NIBS (Dayan *et al* 2013). tDCS and TMS are widely used not only to treat neurological disorders such as depression, epilepsy, Parkinson Alzheimer's disease, and obsessive-compulsive disorder but also to improve memory performance, learning, and other cognitive functions (Nitsche *et al* 2008, Fox *et al* 2014).

Modulation of deep brain structures is rapidly growing as a treatment option for some neurological and psychiatric disorders. Despite current efforts to develop specific coils for TMS such as H-Coil (Roth *et al* 2002), it has not been demonstrated that tDCS and TMS can directly modulate deep brain activity without affecting the overlying cortex (Dayan *et al* 2013). Direct modulation of deep brain structures necessitates invasive techniques such as deep brain stimulation (DBS) (Polanía *et al* 2018). The main purpose of DBS is modulation of neural activities with electric fields in a controlled manner (Kringelbach *et al* 2007). It was approved by the Food and Drug

Administration (FDA) for essential tremor, Parkinson Alzheimer's disease, dystonia, and obsessive-compulsive disorder in 1997, 2002, 2003 and 2009, respectively (Oluigbo *et al* 2012). It also has shown promise for treating additional disorders such as epilepsy, Alzheimer Alzheimer's disease, Tourette Alzheimer's syndrome, addiction, and depression (Oluigbo *et al* 2012).

The clinical success of DBS depends not only on the precise implantation of electrodes into deep brain target tissues, which is recently improved through neuroimaging methods and microelectrode recordings (Gmel *et al* 2015), but also the accurate adjustment of stimulation parameters (Peña *et al* 2017). Consequently, improving DBS lead design (Cubo *et al* 2016) and systematic optimization of stimulation parameters are essential to increase therapeutic effects and decrease side effects (Anderson *et al* 2018). In the other words, DBS therapy is dependent on the spatial distribution of the stimulation fields (which are represented by electric potential (Miocinovic *et al* 2009, Chaturvedi *et al* 2010), electric field (Cubo *et al* 2018) and the second difference of the electric potential (Butson and McIntyre 2008)) in the brain (Åström *et al* 2015). Therefore, the first step to precisely control and anticipate the clinical results of DBS is to compute electric potential and field distributions generated in the brain tissue accurately (Miocinovic *et al* 2009). In addition, developing automatic methods for adjusting the stimulation parameters and predicting the volume of tissue activated (VTA) to achieve the best clinical results can be obtained through computational analysis such as training an artificial neural network (ANN) (Chaturvedi *et al* 2013), convex optimization (Anderson *et al* 2018) and particle swarm optimization (Peña *et al* 2017).

There are several methods to model brain tissue, from homogeneous cylinders and spheres (Walckiers 2009, Grossman *et al* 2017) to precise models considering heterogeneity and anisotropy (Chaturvedi *et al* 2010, Åström *et al* 2012, Gunalan *et al* 2017). Spatial distribution of the electric field in simple models can be computed analytically. However, in more realistic and accurate models, numerical analysis such as finite element method (FEM) should be used. The analytical method is often more accurate and faster than the numerical one. It provides deep insight into electric potential and field distributions and the impact of stimulation parameters on them in the brain tissue to obtain the desired outcomes. In order to obtain the effects of electric field distribution on the neurons, macroscopic (Cubo *et al* 2018) or microscopic models (McIntyre *et al* 2002) can be used. While in the former models, electric potential or its first and second spatial derivatives thresholds are used to determine VTA, in the later ones, compartmental axon cable models are developed for that purpose. Although the microscopic models are more precise, they need more computational power and time. As a result, they are often used to identify activation threshold levels for macroscopic ones (Åström *et al* 2015).

Since different neurons have different excitability properties, the interaction between them and extracellular stimulation is complex. Consequently, the biological mechanisms of neuromodulation methods such as tDCS, TMS, and DBS are not fully known (Cubo *et al* 2018) and analyzing many factors is required to understand the effects of a given brain stimulation. Among different excitability properties, it is demonstrated that there is low-pass filtering behavior in the neurons' membrane due to its leak conductance and capacitance (Hutcheon and Yarom 2000). This behavior generally exists among neurons; however, it depends on several parameters including the axon cable model properties and the input current or voltage characteristics (amplitude and frequency). Based on this low-pass filter behavior and the inception of interferential currents (IFC) therapy, a new non-invasive strategy for electrically stimulating deep regions in the brain was introduced by Grossman *et al* (2017). IFC is a commonly used method in physiotherapy for controlling pain and incontinence, enhancing blood flow and reducing edema and neurological impairments (Goats 1990, Ward 2016). It uses two pairs of medium-frequency currents (carrier frequency) which are slightly different (e.g. 2000 and 2010 Hz). Interfering these two high frequency signals with each other produces an amplitude modulated electric field oscillating at the difference frequency and may be able to stimulate the neurons (Agharezaee and Mahnam 2015). Using *in vivo* experiments on transgenic mice in Grossman *et al* (2017), the authors showed that hippocampal neurons could be stimulated without activating the overlying cortical ones. There are several challenges associated with the noninvasive deep brain stimulation (NDBS) method which have not been solved yet. One of them is to determine the accurate activated area using microscopic models and identify the exact response of the neurons to the modulated electric field. Manual adjustments of stimulation parameters (electrode position, electrode dimensions, and boundary conditions) which were done to achieve the desired electric potential and field distributions limit the efficiency of this method. As a result, developing automatic methods would be necessary to maximize its impacts.

In the present study, we model brain tissue as infinite homogeneous cylinder (IHC) and infinite inhomogeneous cylinder (IIC). We propose analytical solutions in order to not only provide deep insight into the physics of this method but also compute electric potential and field distributions accurately. After determining the activated area in the models through macroscopic approaches, the exact relationship between stimulation parameters and the activated area are extracted. Two automatic methods based on ANN are proposed to adjust the stimulation parameters with two and four electrode pairs in the homogeneous model. Finally, the compartmental axon cable model is developed to analyze the responses of the neurons to the modulated electric field and determine the activated area in homogeneous and inhomogeneous models more accurately (microscopic approach).

## 2. Methods

### 2.1. Forward problem

Analytical and numerical methods are used to compute the electric potential and field distributions in the brain tissue. The IHC and IIC models were developed for brain tissue modeling. Figures 1(a) and (b) show the developed IHC model with two and four electrode pairs, respectively. The configuration of electrodes are determined through the electrode arc length and the angle between its center and $x$ axis. The same method is used to determine the configuration of electrodes in IIC model (figure 1(c)). The infinity of cylinder in the $z$ direction results in the infinity of electrodes in this direction. It can be assumed that each infinite-length electrode is composed of an infinite number of finite-length electrodes ($H = 0.25$ mm in this research) as illustrated in figure 1(d) and $I_i(f_i)$ is applied to each finite-length electrode. So with uniform current distribution approximation, the current density ($\vec{J}$) at each electrode is $I_i(f_i)/S$ where $S$ is the area of the finite height electrode. $I_1$ and $I_2$ currents are applied at $f_1$ and $f_2 = f_1 + \Delta f$, respectively; $f_1$ is above the frequency that neurons can follow due to their intrinsic low-pass filter behavior but $\Delta f$ falls within the responsive neurons frequency range.

#### 2.1.1. Analytical solution

Spatial distribution of electric potential in the brain tissue is determined through solving the quasi-static Laplace equation (Cheng *et al* 1989):

$$\nabla \cdot (\sigma \nabla \varphi) = 0 \tag{1}$$

where $\sigma$ is the electrical conductivity of the brain tissue, $\varphi$ is the electric potential and $\nabla$ is the gradient operator. After finding the electric potential, the electric field ($\vec{E}$) and $\vec{J}$ are obtained as follows (Cheng *et al* 1989):

$$\vec{E} = -\nabla \varphi \tag{2}$$

$$\vec{J} = \sigma \vec{E}. \tag{3}$$

The surrounding boundary is treated as an insulator, i.e. the normal component of current density equals to zero except where the electrodes are located. Under uniform current distribution assumption, the normal component of current density and electric field are obtained by means of (2) and (3).

In an IHC with radius $\rho_0$ and conductivity $\sigma_0$, the solution of (1) in cylindrical coordinate system is (Cheng *et al* 1989):

$$\varphi(\rho, \phi) = \sum_{n=1}^{\infty} \rho^n (E_n \cos n\phi + F_n \sin n\phi) \tag{4}$$

where $E_n$ and $F_n$ are obtained through boundary conditions. According to the previous description, the boundary conditions are Neumann type, i.e. $\vec{J}.\vec{n} = 0$ ($\vec{n}$ is the outward unit vector normal to the line element) in all surrounding boundaries except at the electrodes' positions. In these areas we have:

$$\frac{\partial \varphi}{\partial \rho} = -\frac{\vec{J}.\vec{n}}{\sigma_0}. \tag{5}$$

The unknown coefficients in (4) then are found as (Cheng *et al* 1989):

$$E_n = \frac{\int_0^{2\pi} \frac{\partial \varphi}{\partial \rho} \mid_{\rho=\rho_0} \cos n\phi d\phi}{n\rho_0^{n-1}\pi} \tag{6}$$

$$F_n = \frac{\int_0^{2\pi} \frac{\partial \varphi}{\partial \rho} \mid_{\rho=\rho_0} \sin n\phi d\phi}{n\rho_0^{n-1}\pi}. \tag{7}$$

This solution is valid under the establishment of the compatibility condition which is one of the results of Green's second identity (Balanis 1999). Based on the above constraint, it is essential that:

$$\int_0^{2\pi} \frac{\partial \varphi}{\partial \rho} \mid_{\rho=\rho_0} d\phi = 0 \tag{8}$$

which means that each electrode pair must have the same arc length.

The next model for the brain tissue is the infinite-centric cylinder of $N$ layers with different conductivities (figure 1(c)). In this model, the Laplace equation in each layer should be solved. According to continuity of potential and normal component of current density at the interface between two layers and based on the most

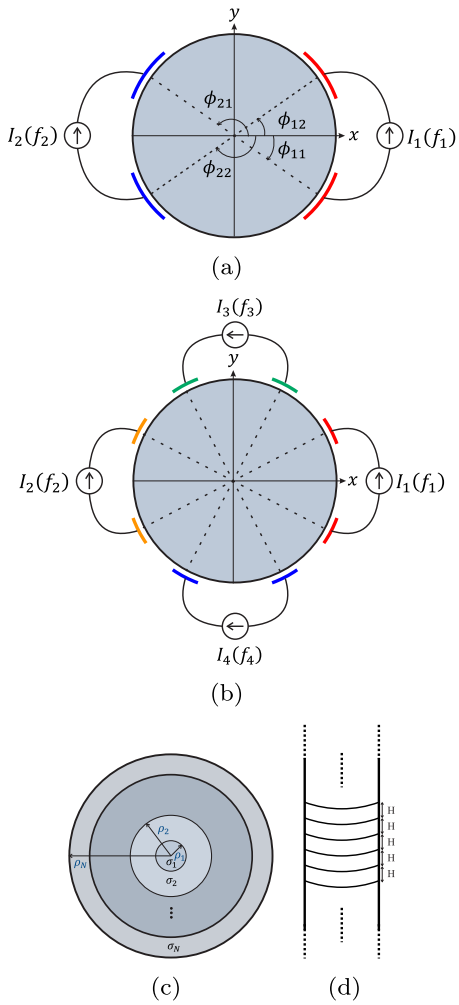


**Figure 1.** (a). IHC with two electrode pairs. (b). IHC with four electrode pairs. (c). IIC which configuration of electrodes are determined the same as IHC. (d). Infinite electrode model.

inner layer coefficients, the recursive relationship is computed. In the most inner layer, the solution of Laplace equation is the same as (4) and in $i$th layer ($i \geqslant 2$) we have (Cheng *et al* 1989):

$$\varphi(\rho,\phi) = \sum_{n=1}^{\infty} \left(A_n^i \rho^n + B_n^i \rho^{-n}\right) \left(C_n^i cosn\phi + D_n^i sinn\phi\right) \tag{9}$$

where

$$\begin{aligned} A_n^i &= 1 \\ B_n^i &= \frac{w-1}{w+1}\rho_{i-1}^{2n} \\ \frac{C_n^i}{E_n} &= T^i = \frac{w+1}{2w}\left(1 + B_n^{i-1}\rho_{i-1}^{-2n}\right) T^{i-1}, T^1 = 1 \\ \frac{D_n^i}{F_n} &= T^i \end{aligned} \tag{10}$$

and

$$w = \frac{\sigma_i}{\sigma_{i-1}} \frac{1 + B_n^{i-1}\rho_{i-1}^{-2n}}{1 - B_n^{i-1}\rho_{i-1}^{-2n}} \tag{11}$$

where $\sigma_i$ is the electrical conductivity in $i$th layer, $\rho_i$ is the external radius of $i$th layer, and the unknown coefficients ($E_n$ and $F_n$) are obtained by means of boundary condition at $\rho = \rho_N$ (Cheng *et al* 1989):

$$E_n = \frac{\int_0^{2\pi} \frac{\partial \varphi}{\partial \rho} \mid_{\rho=\rho_N} \cos n\phi d\phi}{n\left(\rho_N^{n-1} - B_n^N \rho_N^{-n-1}\right)\pi} \tag{12}$$

$$F_n = \frac{\int_0^{2\pi} \frac{\partial \varphi}{\partial \rho} \mid_{\rho=\rho_N} \sin n\phi d\phi}{n\left(\rho_N^{n-1} - B_n^N \rho_N^{-n-1}\right)\pi}. \tag{13}$$

It is obvious from (6), (7), (12) and (13) that the potential distribution in the brain tissue is dependent on the configuration of electrodes and boundary conditions. Therefore, we can alter the electric potential and field distribution by changing these parameters in a controlled manner.

Since the boundary conditions are time-dependent, the electric field generated in the brain tissue changes spatially and temporally. In temporal interference (TI) stimulation, modulation envelope amplitude (MEA, i.e. the difference between the maximum and minimum value of the modulated electric field Alzheimer's envelope) is an important parameter. MEA is a time-independent parameter (in a specific location in a model with fixed boundary conditions (see figure S1)) and can be obtained by using phasor electric fields. For any electrode pair with a given frequency, we compute the phasor electric potential and field distribution by using the mentioned analytical solution method. If there are only two electrode pairs, accurate electric field MEA generated by TI of electric fields will be calculated as follows (Grossman *et al* 2017):

$$\begin{aligned} |\overrightarrow{E}_{AM}(\overrightarrow{n},\overrightarrow{r})| = &\left|\left(\overrightarrow{E}_1(\overrightarrow{r}) + \overrightarrow{E}_2(\overrightarrow{r})\right)\cdot\overrightarrow{n}\right| \\ &- \left|\left(\overrightarrow{E}_1(\overrightarrow{r}) - \overrightarrow{E}_2(\overrightarrow{r})\right)\cdot\overrightarrow{n}\right| \end{aligned} \tag{14}$$

where $\overrightarrow{E}_1(\overrightarrow{r})$ and $\overrightarrow{E}_2(\overrightarrow{r})$ are the phasor electric fields generated by two electrode pairs, $\overrightarrow{r}(x,y,z)$ is the specific location and $\overrightarrow{n}$ is the unit vector of the desired direction. Furthermore, $|E_{AM}^{max}(\overrightarrow{r})|$ is the maximum electric field MEA across all directions and is obtained analytically as follows (Grossman *et al* 2017):

$$|E_{AM}^{max}(\overrightarrow{r})| = \begin{cases} 2|\overrightarrow{E}_2(\overrightarrow{r})| & |\overrightarrow{E}_2(\overrightarrow{r})| < |\overrightarrow{E}_1(\overrightarrow{r})|\cos(\theta) \\ 2|\overrightarrow{E}_2(\overrightarrow{r})|\sin(\gamma) & otherwise \end{cases} \tag{15}$$

where $\theta$ is the angle between $\overrightarrow{E}_1(\overrightarrow{r})$ and $\overrightarrow{E}_2(\overrightarrow{r})$ and is smaller than $\pi/2$ and $\gamma$ is the angle between $\overrightarrow{E}_2(\overrightarrow{r})$ and $\overrightarrow{E}_1(\overrightarrow{r}) - \overrightarrow{E}_2(\overrightarrow{r})$ with $|\overrightarrow{E}_1(\overrightarrow{r})| > |\overrightarrow{E}_2(\overrightarrow{r})|$ assumption. For $m$ electrode pairs ($m > 2$), MEA at the desired direction and its maximum across all direction are approximated by (Grossman *et al* 2017):

$$\begin{aligned} &|\overrightarrow{E}_{AM}(\overrightarrow{n},\overrightarrow{r})| \\ &= 2\,min\{|\overrightarrow{E}_1(\overrightarrow{r})\cdot\overrightarrow{n}|, |\overrightarrow{E}_2(\overrightarrow{r})\cdot\overrightarrow{n}|, ..., |\overrightarrow{E}_m(\overrightarrow{r})\cdot\overrightarrow{n}|\} \end{aligned} \tag{16}$$

$$\begin{aligned} &|E_{AM}^{max}(\overrightarrow{r})| \\ &= 2\,min\{|\overrightarrow{E}_1(\overrightarrow{r})|, |\overrightarrow{E}_2(\overrightarrow{r})|, ..., |\overrightarrow{E}_m(\overrightarrow{r})|\}. \end{aligned} \tag{17}$$

*2.1.2. Numerical solution using FEM*

The finite element models of NDBS are created to evaluate the accuracy of our analytical solution results. IHC and IIC are constructed with approximately 25 000 elements, and stimulation parameters are set the same as analytical solutions. By using these models, (1) is solved for each geometry to compute electric potential and field distributions.

### 2.2. Inverse problem

In section 2.1, spatial distributions of the potential and electric field in IHC and IIC were computed based on the specific boundary conditions to determine the activated area. In order to activate the desired region in the model, we have to solve the inverse problem (determining boundary conditions).

In this paper, we use ANN to solve the inverse problem in the IHC with 50 mm diameter cylinder. The maximum MEA of the electric field is used to determine the activated area through the macroscopic approach, since it is less sensitive to stimulation parameters compared to other quantities (Åström *et al* 2015).

First, two fixed and symmetrical electrode pairs were used with the following parameters: $\phi_{11} = -25°$, $\phi_{12} = 25°$, $\phi_{21} = 155°$, $\phi_{22} = -155°$, and 10° arc length for all electrodes (see figure 1(a)). The size and position of the activated area are controlled only by means of the current sum ($I_1 + I_2$) and the current ratio ($I_2/I_1$). The symmetry of the stimulation parameters in $x$ axis causes the center of gravity (COG) of the activated area to be on $x$ axis in all datasets. However, the location of the activated area can be moved to the desired location by the appropriate rotation of the coordinate system. In the other words, it is enough to create an ANN to determine the stimulation parameters for activating a desired region that it is located on the $x$ axis. Through simple pre-processing (appropriate rotation of the coordinate system) and post-processing (back to the original coordinate system), we can solve the inverse problem for any activated area in the model. To create a dataset for ANN, current sum and current ratio are systematically increased from 0.5 mA to 3 mA in steps of 0.1 mA and from 1 to

10 in steps of 0.1, respectively. As we will discuss in section 3.1, the location of the activated area moves toward the first electrode pair (positive $x$ axis in our configuration) when we change the current ratio for values greater than one. It would be sufficient based on our previous description about the coordinate system rotation. For each trial in the dataset, the activated area is determined by using 193 V m$^{-1}$ threshold. To determine the threshold for macroscopic approach, the neuron anatomy and the pulse characteristics should be included. To the best of our knowledge, the proposed thresholds were have not been calculated by using TI stimulation (McIntyre *et al* 2002, Åström *et al* 2015). The 193 V m$^{-1}$ threshold is used as an example which makes the activated area a connected space when 1 mA current is applied to the electrodes. It should be noted that the trials in which the activated area is empty or not a connected space has been removed from the dataset. Then, the $x$ and $y$ coordinate of the COG of the activated area ($x_c$ and $y_c$), and the Euclidean distance between the COG and point 1 ($R_y$, see figure 2(a)) are determined for the whole dataset. As mentioned previously, $y_c$ is close to zero in all trials. In addition, the Euclidean distances between the COG and other contour points are highly correlated to $R_y$. For instance, the correlation coefficient between $R_x$ (the Euclidean distance between the COG and point 2, see figure 2(a)) and $R_y$ is 0.952. As a result, neither the Euclidean distances between the COG and other contour points nor $y_c$ are appropriate inputs for the ANN. Therefore, the first ANN receives $x_c$ and $R_y$ as inputs and computes the current ratio and the current sum as outputs (figure 2(d)).

Several approaches help us to control the shape of the activated area more desirably and overcome some existing limitations. Generating TI electric fields with more than two electrode pairs is one of these methods. As the number of electrode pairs increases, the shape of the activated area becomes more controllable. For instance, $R_x$ and $R_y$ become independent by using four electrode pairs. Thus in the second step, four fixed and symmetrical electrode pairs with $\phi_{11} = -25°$, $\phi_{12} = 25°$, $\phi_{21} = 155°$, $\phi_{22} = -155°$, $\phi_{31} = 65°$, $\phi_{32} = 115°$, $\phi_{41} = -115°$, $\phi_{42} = -65°$, and 10° arc length for all electrodes (see figure 1(b)) are used; and the current sum and the current ratio for each electrode pair ($I_1 + I_2$ and $I_2/I_1$ for first and second electrode pairs, and $I_3 + I_4$ and $I_4/I_3$ for third and fourth electrode pairs) can be changed. To create a dataset, $I_1 + I_2$ and $I_3 + I_4$ are systematically increased from 0.5 mA to 3 mA in steps of 0.1 mA, and $I_2/I_1$ is increased from 1 to 10 in steps of 0.1 while keeping $I_4/I_3$ fixed at 1. In this manner, the position of the activated area is changed only on the positive $x$ axis, the same configuration with two electrode pairs.

The second ANN receives $x_c$, $R_x$, and $R_y$ as inputs and computes $I_2/I_1$, $I_1 + I_2$, and $I_3 + I_4$ as outputs (figures 2(b) and (e)). In the same way, $y_c$ is close to zero in all trials, thus it is not an appropriate input for ANN. In this dataset, the correlation coefficient between $R_x$ and $R_y$ is 0.2575 which demonstrates that they are independent, as we expected.

Two multi-layer perceptron (MLP) ANNs with two and three layers are used to estimate the outputs (see figure 2). The number of neurons is set equal in the hidden layers of each ANN and it is changed from 1 to 15. The best number of hidden neurons which leads to minimum mean square error (MSE) on the test data is 11 and 14 for the first and second ANNs, respectively. The sigmoid function is used for the hidden neurons and the linear function for the output neurons.

The Levenberg–Marquardt algorithm (Marquardt 1963) is used to train the neural networks. Training stops when six sequential increases of error occur on a randomly selected validation dataset. The *k-Fold*($k = 10$) cross validation method is used to evaluate the developed ANNs. To do this, all the samples in the dataset are split into $k$ non-overlapping subsets. One subset is used as the test data, 80% of the remaining samples ($k$-1 subsets) are used to train the network (training data), and 20% of them are randomly selected as the validation set to avoid overfitting of the network. This process is repeated $k$ times and the MSE of the estimations for the test data is calculated. To better evaluate the developed ANNs, the actual activated area and the predicted one are compared using specificity, sensitivity, and the Jaccard index (a statistical parameter for comparing the similarity of two shapes, with a range from 0 to 1). There are targets and outputs (ANNs estimation) for each individual sample in the test data. The actual activated area and the predicted one are computed using targets and outputs, respectively. After calculating false-positive (FP, type I error), false-negative (FN, type II error), true-positive (TP, power) and true-negative (TN), the specificity, sensitivity, and Jaccard index are obtained using (18) through (20). FP corresponds to spatial regions where the predicted activated area goes beyond the actual activated area. Conversely, FN resulted from the condition where the predicted activated area is smaller than the actual one. Figure 3 shows the scientific workflow for development of the inverse problem solution in IHC with two electrode pairs. The similar workflow is done for configuration with four electrode pairs.

$$specificity = \frac{TN}{TN + FP} \tag{18}$$

$$sensitivity = \frac{TP}{TP + FN} \tag{19}$$

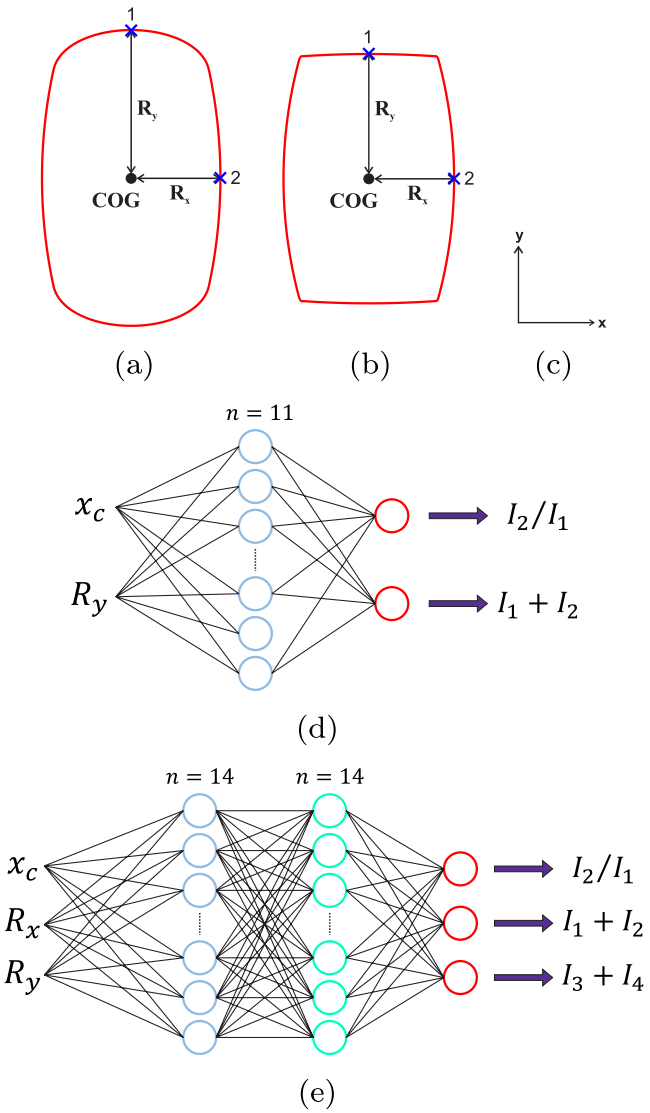


**Figure 2.** (a) The activated area with two electrode pairs. (b) The activated area with four electrode pairs. (c) Coordinate system (d) ANN architecture for the current ratio and the current sum estimation for configuration with two electrode pairs. (e) ANN architecture for the current ratio and the current sums estimation for configuration with four electrode pairs.

$$Jaccard\ index = \frac{TP}{TP + FP + FN}. \tag{20}$$

### 2.3. Axon modeling

The electrical behavior of the neuron is modeled to determine axonal activation in response to TI stimulation (a kind of extracellular stimulation). To investigate the ability of neurons to demodulate and follow the envelope modulated electric field which results in generating action potentials (APs) just in deep regions rather than in overlying ones, a computational axon cable model is developed. The basis of extracellular electrical stimulation of axons was described in Rattay (1986) and Richardson *et al* (2000).

The electrical response of the axon is given by (Rattay 1986):

$$\frac{dV_n}{dt} = (G_a(V_{n-1} - 2V_n + V_{n+1} + V_{e,n-1} - 2V_{e,n} + V_{e,n+1}) - I_{i,n})/C_m \tag{21}$$

where

$$V_n = V_{i,n} - V_{e,n} + V_r \tag{22}$$

and $V_{i,n}$ is the intracellular potential, $V_{e,n}$ is extracellular potential (generated by electrodes) at the $n$th node of Ranvier and $V_r$ is the resting potential. $I_{i,n}$ describes ionic currents at $n$th node of Ranvier. It is a function of $V_n$

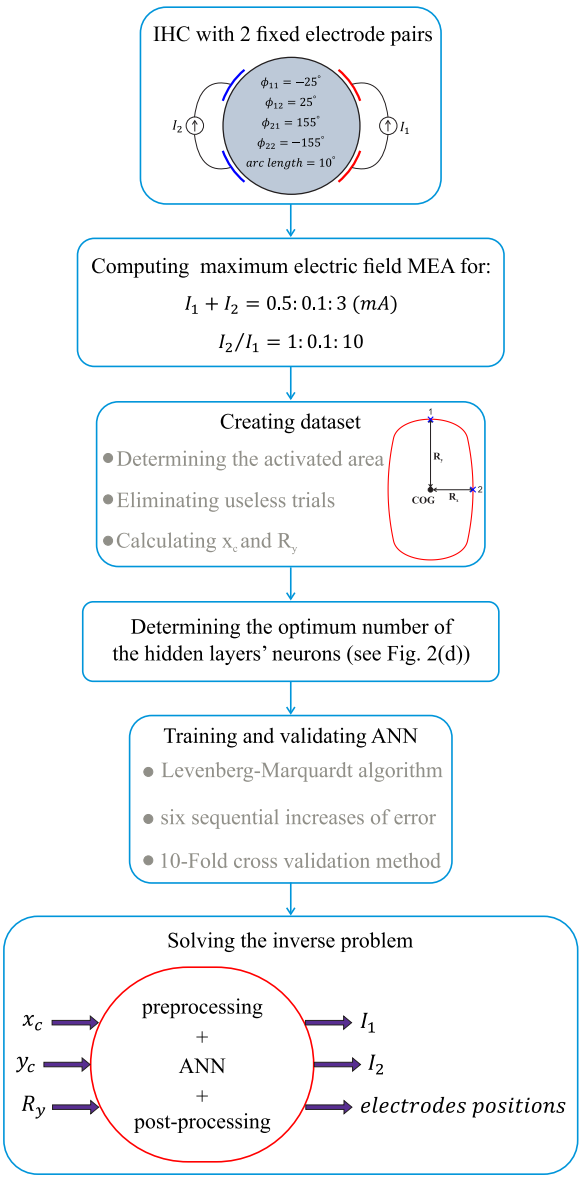


**Figure 3.** Block diagram of the solution of the inverse problem in IHC with two electrode pairs. The block diagram for configuration with four electrode pairs is similar to this one.

and time (t) and is modeled by Hodgkin–Huxley (HH) differential equations (Hodgkin and Huxley 1952). $C_m$ is the nodal capacitance, and $G_a$ is the axial conductance which is given by:

$$G_a = \frac{1}{r_s \Delta l} \tag{23}$$

where $\Delta l$ is node to node interval and $r_s$ is:

$$r_s = \frac{4\rho_i}{\pi d^2} \tag{24}$$

where $\rho_i$ is the resistivity of axoplasm and $d$ is axon diameter. The developed axon cable model has 11 nodes of Ranvier according to Raspopovic *et al* (2011). In our model (similar to the 'model A' which was developed by Richardson *et al* (2000)), the myelin is treated as a perfect insulator (Richardson *et al* 2000); so, the membrane dynamics of the nodes of Ranvier describe the behavior of the model. In other words, the equivalent circuit of the Ranvier nodes (or ion currents) are connected to one another by a resistance representing axoplasm. The dynamic of ion channels in the developed model is described by differential equations (Hodgkin and Huxley 1952). These equations along with the geometrical and electrical parameters of the developed axon cable model are presented in section 1 of the supplementary material (stacks.iop.org/PMB/64/235010/mmedia).

The activating function (AF), the second spatial difference of $V_e$ in (21), is responsible for the activations in the axon (Rattay 1986). It should be noted that for the first and last nodes of Ranvier, the second spatial difference changes to the first spatial difference of $V_e$. We investigated the axonal activation in response to TI

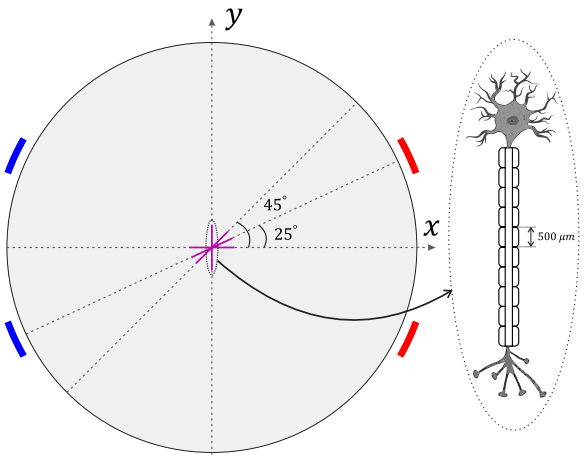


**Figure 4.** The modeled axons (purple lines) at all desired directions in the center of the infinite cylinder with two electrode pairs (red and blue). You can see the geometric structure of the axon cable model associated with each purple line in this image. The angle between the center of electrodes and the $x$ axis are $-25°, 25°, 155°$, and $-155°$ and the arc length of all electrodes is $10°$.

stimulation; The activated area through microscopic approach in IHC and IIC with 50 mm diameter was determine based on two electrode pairs with equal currents. The configuration of electrodes are fixed and symmetrical ($\phi_{11} = -25°, \phi_{12} = 25°, \phi_{21} = 155°, \phi_{22} = -155°$, and the arc length of all electrodes$= 10°$); consequently, the generated electric potential is maximum in deep structures and minimum in surface ones. The developed axon cable model is oriented in four directions ($\phi = 0°, 25°, 45°$, and $90°$) for each point in the model (see figure 4). $25°$ is the angle between the $x$ axis and the line that connects the center of the electrodes located in the first and third quarter of the coordinate system. Due to the symmetry of the problem, considering the direction of the axon cable model in the first quarter of the coordinate system is enough. After computing the phasor electric potential for each electrode pair, phasor AF at a desired direction is calculated ($AF_1$ and $AF_2$ for the first and second electrode pairs). Then, AF is computed by means of a relationship similar to (14) for scalar quantities (i. e. $\mathrm{AF} = ||AF_1 + AF_2| - |AF_1 - AF_2||$). After computing AF in a desired direction, the axonal response to TI stimulation is computed at that direction. For this purpose, the equal applied currents to the electrodes are increased until APs are generated in the axon located at the center of the model. The minimum current that produces APs in that axon is called the current threshold (CT) for that particular direction. Subsequently, AF is recalculated in all directions with the minimum of CT while 86 axons are distributed at 4 mm intervals in the model to determine the activated axons. To determine the activated area more accurately, the same procedure is applied to the axons with less interval (1 mm). Finally, the effects of frequencies, $f_1$ and $\Delta f$, on the minimum of CT are investigated in the homogeneous model.

## 3. Results

### 3.1. Forward problem

The electric field distribution in two developed models under the Neumann boundary condition was analytically computed in phasor form for each current source. Subsequently, the electric field MEA for radial and tangential direction and maximum electric field MEA were computed using (14) through (17) based on the number of electrode pairs. For instance, figures 5(a), (c) and (e) show $|\overrightarrow{E}_{AM\hat{\rho}}(x,y)|$, $|\overrightarrow{E}_{AM\hat{\phi}}(x,y)|$, and $|E^{max}_{AM}(x,y)|$, respectively, for configuration with two electrode pairs and figure 5(e) shows $|E^{max}_{AM}(x,y)|$ for configuration with four electrode pairs in the IHC of 50 mm diameter and $\sigma = 0.33$ S m$^{-1}$. Additionally, figure 5(d) shows $|E^{max}_{AM}(x,y)|$ in the infinite cylinder of 50 mm diameter with inhomogeneous conductivity consisting of four layers: scalp ($\rho_4 = 1$, $\sigma_4 = 0.333$ S m$^{-1}$), skull ($\rho_3 = 0.95, \sigma_3 = 0.0083$ S m$^{-1}$), cerebrospinal fluid ($\rho_2 = 0.865, \sigma_2 = 1.79$ S m$^{-1}$), and brain ($\rho_1 = 0.842$, $\sigma_1 = 0.333$ S m$^{-1}$) (Grossman *et al* 2017), where $\rho_i$ is the normalized layer thickness with respect to $\rho_N$, for configuration with two electrode pairs. These figures demonstrate that by choosing the configuration of electrodes appropriately, the maximum MEA will have greater values in the deep regions of the model.

For investigating the influence of inhomogeneity on the spatial distribution of the electric field during TI stimulation, we computed the ratio of $|E^{max}_{AM}(x,y)|$ in the homogeneous model to the inhomogeneous one (see figure S3). The minimum and maximum of this ratio are 0.91 and 1.32, respectively. These results demonstrate that even considering symmetric inhomogeneity can affect the electric field distribution in the infinite cylinder model. According to the previous studies, controlling the electric field distribution in NDBS the same as DBS is a challenging problem.

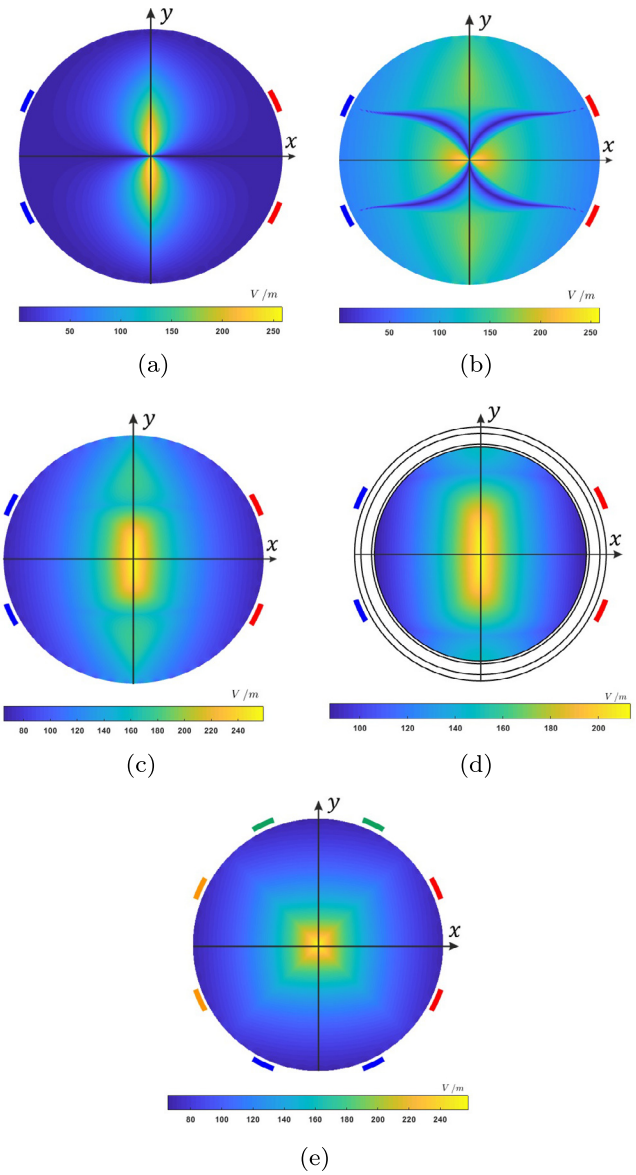


**Figure 5.** (a) Radial electric field MEA ($|\overrightarrow{E}_{AM\hat{\rho}}(x,y)|$), (b) tangential electric field MEA ($|\overrightarrow{E}_{AM\hat{\phi}}(x,y)|$), (c) maximum electric field MEA ($|E^{max}_{AM}(x,y)|$) in an IHC with two electrode pairs (red and blue) that $I_1 = I_2 = 1$ mA. (d) Maximum electric field MEA ($|E^{max}_{AM}(x,y)|$) in the brain of IIC with two electrode pairs (red and blue) that $I_1 = I_2 = 1$ mA. (e) Maximum electric field MEA ($|E^{max}_{AM}(x,y)|$) in the brain of IHC with four electrode pairs (red, green, orange, and blue) that $I_1 = I_2 = I_3 = I_4 = 1$ mA. The angle between the center of electrodes and $x$ axis are $-25°, 25°, -155°$, and $155°$ for two electrode pairs and $-25°, 25°, 65°, 115°, 155°, -155°, -115°$, and $-65°$ for four electrode pairs. The arc length of all electrodes is $10°$.

The maximum relative error between analytical and numerical methods for $|E^{max}_{AM}(x,y)|$ in homogeneous and inhomogeneous models were 5.8% and 4%, respectively. The maximum errors occur at the edge of two developed models due to Gibbs phenomenon. It is the peculiar manner in which the Fourier series of a piecewise continuously periodic function (such as (4)) behave at discontinuities and create overshoots in these locations. The overshoots do not die out as the series is truncated (Pinsky 2008).

From (14), it can be found that MEA at a given direction will maximize where the amplitudes of the electric field generated by each electrode pairs are close together. Thus, the position and dimension of the activated area (the area where the maximum electric field MEA is greater than the given threshold) can change not only with the configuration of electrodes but also with the currents applied to them.

Determining the activated area in the IHC through the macroscopic approach (using 193 V $m^{-1}$ threshold) showed that it is possible to activate the region in the depth of the model without activating overlying ones (see figures S2(a)–(c)). By alternating the current ratio ($I_2/I_1$) from 1 to 2, 4, 6 and keeping the current sum constant, the location of the activated area moves toward the first electrode pair with less injected current because the amplitudes of the electric field generated by each pair of electrodes will be equal at that position. Figure 6 demonstrates this property for $|E^{max}_{AM}(x,y)|$. It shows, for instance, that $x_c$ moves 5.3 mm toward the first electrode pair by doubling the current ratio.

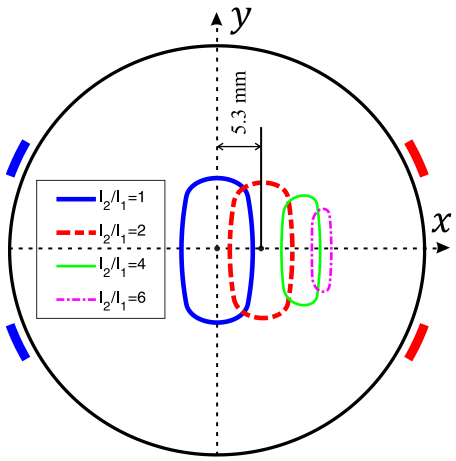


**Figure 6.** Contours of 193 V m$^{-1}$ of $|E_{AM}^{max}(x, y)|$. The configuration of electrodes are the same as two electrode pairs model in figure 5 and the current sum is 2 mA. $I_1$ and $I_2$ are associated with the red and blue electrode pairs, respectively.

**Table 1.** 5-fold cross validation method results.

| | Variable | Order of fitted polynomial | MSE (mm$^2$) |
|---|---|---|---|
| $I_1 + I_2$ is fixed | $x_c$ | 5 | 0.0008 |
| | $R_y$ | 4 | 0.0021 |
| $I_2/I_1$ is fixed | $R_y$ | 4 | 0.0030 |

To investigate further, the exact relationship between stimulation parameters and the activated area was extracted when the configuration of electrodes were fixed the same as two electrode pairs model in figure 5. For this purpose, the activated area in IHC was determined through the macroscopic approach (using 193 V m$^{-1}$ of $|E_{AM}^{max}(x, y)|$ threshold), and $x_c$ and $R_y$ (as the first step in the inverse problem) were computed when $I_2/I_1$ was increased from 1 to 10 in steps of 0.05 while the current sum was kept fixed at 2 mA. As in the *k-Fold* ($k = 5$) cross validation method, 80% of all samples were used to fit the $n$th-degree polynomial functions on the points (($I_2/I_1$, $x_c$) and ($I_2/I_1$, $R_y$) samples). The remaining samples, test data, were used to evaluate the fitted polynomial functions. This process was repeated 5 times and MSE of the test data was calculated; the results are given in table 1. The same procedure was done by systematically increasing $I_1 + I_2$ from 0.5 mA to 3 mA in steps of 0.01 mA and keeping the current ratio fixed at 1 (table 1). Since $x_c$ is zero in all trials, it is not given in the table. The low MSE values of the test data demonstrate that it is possible to control the size and location of the activated area by means of changing stimulation parameters. Consequently, some methods can be developed to solve the inverse problem.

Several other parameters can change the size and location of the activated area such as the arc length of the electrodes and the electrodes' positions (for instance asymmetrical configuration of electrodes); however, we do not focus on them because these changes are not as easy as applied currents to the electrodes.

### 3.2. Inverse problem

By changing the current sum and current ratio of the applied currents to the electrodes, two datasets were created. These datasets are associated with two and four electrode pairs with 474 and 15 755 samples, respectively. Nonlinear regression between inputs and outputs was performed to solve the inverse problem using two ANNs. Figure 2 shows the inputs and outputs of each ANNs. As we mentioned in section 2.2, the activated area in each trial was obtained with 193 V m$^{-1}$ of $|E_{AM}^{max}(x, y)|$ threshold through the macroscopic approach. The neuron anatomy and the applied current characteristics have not been included in the aforementioned threshold. If the actual threshold is kV m$^{-1}$, the current sum and current ratio which are estimated by the proposed method for activating a desired location should be multiplied by $k$/193. It is because of the linear relationship between the boundary condition and the electric field distribution in our developed models.

The MSE values were obtained between targets and estimations in the test data. Also, for better evaluation of two developed ANNs, the specificity, sensitivity and Jaccard index were calculated between the actual activated area and predicted one, and the Mean and SD of these parameters and the MSE of the test data for each developed ANN are given in table 2. The values demonstrate that the stimulation parameters can be obtained accurately according to a desired activated area. Also, the Mean and SD of errors between targets and estimations in the test data are given in table 2. According to these results, both ANNs perform well in estimating the outputs since the

**Table 2.** The statistical parameters for evaluating two developed ANNs in the homogeneous model. The geometries are the same as figures 5(e) and (h) for the first and second ANNs, respectively.

| | | | Error | Sensitivity | Specificity | Jaccard index |
|---|---|---|---|---|---|---|
| | Output | MSE | (Mean ± SD) | (Mean ± SD) | (Mean ± SD) | (Mean ± SD) |
| 1st ANN | $I_2/I_1$ | $1.73 \times 10^{-4}$ | $-1.26 \times 10^{-4} \pm 0.0125$ | $0.9955 \pm 9.24 \times 10^{-4}$ | $0.9952 \pm 0.0010$ | $0.9654 \pm 0.1125$ |
| | $I_1 + I_2$ | $3.172 \times 10^{-5}$ (mA$^2$) | $6.32 \times 10^{-5} \pm 0.0033$ | | | |
| 2nd ANN | $I_2/I_1$ | 0.0924 | $-4.89 \times 10^{-4} \pm 0.3065$ | | | |
| | $I_1 + I_2$ | 0.0138 (mA$^2$) | $-2.02 \times 10^{-4} \pm 0.1179$ | $0.9926 \pm 8.33 \times 10^{-4}$ | $0.9925 \pm 7.19 \times 10^{-4}$ | $0.9440 \pm 0.1125$ |
| | $I_3 + I_4$ | 0.0033 (mA$^2$) | $2.08 \times 10^{-5} \pm 0.0570$ | | | |

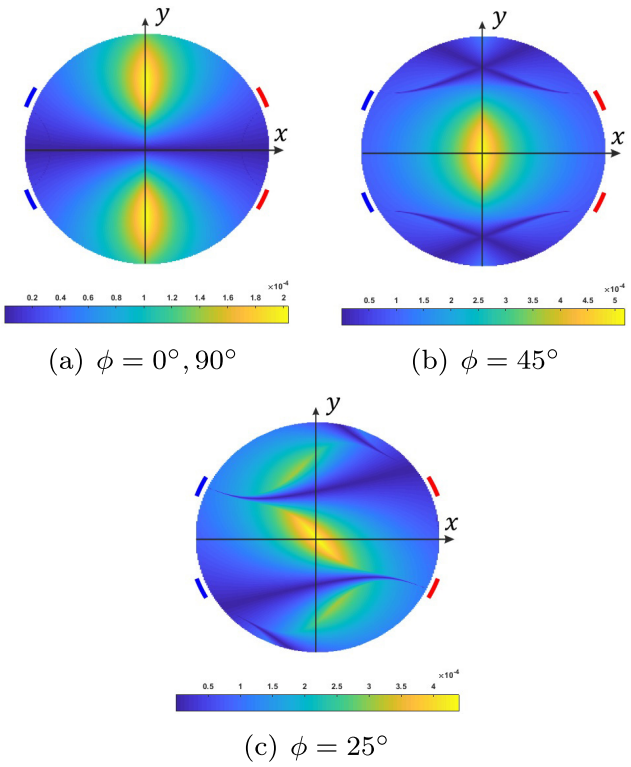


**Figure 7.** Second spatial difference of the electric potential in four directions for the homogeneous model with two electrode pairs that $I_1 = I_2 = 0.5$mA, all values are in volt. The angle between the center of electrodes and $x$ axis are $-25°, 25°, -155°$, and $155°$ and the arc length of all electrodes is $10°$. (a). $\phi = 0°, 90°$. (b) $\phi = 45°$. (c) $\phi = 25°$.

Mean is near zero and the SD is small (figure S4 shows error histograms). Although the results demonstrate that the first ANN is better than the second one, it is possible to control the activated area more desirably in the second method.

### 3.3. Axon modeling

A compartmental axon cable model was used to investigate if electric potential distribution generated by the electrodes can generate APs only in neurons located in the deep region and to determine the responses of the neurons to the modulated electric field.

AF was obtained in four directions in IHC and IIC (see figure 7). The AF values in the deep structures of 45° direction are more than twice the maximum values for 0° and 90° directions in the surface regions. The current threshold (the minimum current in which the axon located in the center of the model spikes in every cycle of the input signal) for four mentioned directions was computed while $f_1 = 2500$ Hz and $\Delta f = 20$ Hz. The results are given in table 3 for the homogeneous and inhomogeneous models.

AF values in four directions with the minimum CT (160 $\mu$A for the homogeneous model and 192 $\mu$A for the inhomogeneous one) were obtained again. AF values can only activate axons at depth of 90° direction (see figures 8(a) and (b)). Although the maximum values of the second spatial difference of electric potential in $\phi = 0°$, 90° (at surface regions) and in other directions (at deep regions) are greater than the values that generated APs in the mentioned axons (at 90°), these maximum values cannot activate the axons in the model.

**Table 3.** Current threshold for four directions in IHC and IIC with two electrode pairs. The geometries are the same as two electrode pairs model in figure 5. The injected current is increased from 0 $\mu$A to 1500 $\mu$A with 1 $\mu$A step.

| | CT ($\mu A$) | |
|---|---|---|
| Direction | Homogeneous | Inhomogeneous |
| 0° | [a] | [a] |
| 90° | 160 | 192 |
| 45° | 222 | 269 |
| 25° | 370 | 452 |

[a]No APs generated.

However, the first spatial difference of the electric potential at the first and last nodes of the stimulated axons is great enough to activate them. These results demonstrate that similar to the macroscopic approach, the activated area is a connected space and has been located at deep regions of the model.

Figures 8(c) and (d) show the activated area in the homogeneous and inhomogeneous models at $\phi = 90°$ to more accurately investigate the spatial resolution of stimulation. Despite our expectation, the activated areas computed using the macroscopic (figure 6 in section 3.1) and microscopic approaches are not similar. A possible reason is that AF is computed only in four directions. Figure 8 shows the differences between the homogeneous and inhomogeneous models. Although the geometric properties of the developed axon cable model affect the reported results (such as CT), similar results can be yielded using other geometrical properties. For instance, by using 1000 $\mu$m and 1500 $\mu$m node to node separation, minimum CT in four directions will be 82 $\mu$A and 52 $\mu$A, respectively. Therefore, CT decreases as the node to node separation increases, which is in agreement with the results of rectangular pulse DBS (Åström *et al* 2015).

The low-pass filtering behavior in the membrane of neurons depends on the axon cable model, the input current characteristics (amplitude and frequency), and the instant voltage of the membrane. We found that the developed axon cable model cannot follow the frequencies higher than 2500 Hz. Figure 9 illustrates the electrical response of the axon to the modulated electric field in the homogeneous model. Unlike axons stimulated with $\Delta f = 50$ Hz, no APs were observed in the axons stimulated with $\Delta f = 0$. These results indicate that the axon does not follow high frequency components of the input signal; however, it seems that the axon follows the envelope of the signal.

At the end of this section, the effects of $\Delta f$ and $f_1$ on CT were evaluated in the homogeneous model. $\Delta f$ was increased from 10 Hz to 100 Hz in steps of 10 Hz while keeping $f_1$ fixed at 2500 Hz and $f_1$ was increased from 2500 Hz to 6000 Hz in steps of 500 Hz while keeping $\Delta f$ fixed at 50 Hz. In all cases, AF (in $\phi = 90°$) was computed and applied to the axon located at the center point of the model. The results are represented in table 4. CT decreases as $\Delta f$ increases from 10 Hz to 60 Hz, and then increases as $\Delta f$ reaches 100 Hz (table 4. A). A possible reason is that there is a resonance in the electrical response of neurons (Hutcheon and Yarom 2000). On the other hand, while $f_1$ increases from 2500 Hz to 6000 Hz, CT increases continuously (table 4. B). These computational results are in agreement with practical ones reported in the literature (Grossman *et al* 2017). It is obvious that the MEA of the input signal does not depend on $\Delta f$ or $f_1$; however, since the axon cable model is time-dependent, such properties affect the model response and consequently CT.

## 4. Discussion

The brain tissue was modeled as IHC and IIC and the electric field and potential distributions were computed analytically to better understand how this technique works. Since there is a linear relationship between electric field strength and the dimension of the model, our results are compatible with all other diameters. For instance, if the diameter of the model is $a$ mm while keeping all other parameters constant, the strength of the electric field distribution which is computed by the 50 mm diameter should be multiplied by $50/a$. Therefore, increasing model size decreases the electric field strength and it is a challenge associated with using NDBS in the human brain. The effects of stimulation parameters on electric field distribution and the activated area were quantified. We showed that the activated area can be moved either by changing the electrodes' positions or the ratio of applied currents to them in a quantified manner. The heterogeneity and anisotropy of brain tissue, which have been investigated in several studies (Åström *et al* 2012, Howell and McIntyre 2016), affect electric potential and field distributions in DBS. In NDBS, we consider inhomogeneity with cylindrical symmetry in infinite cylinder because only in this way, can the problem be solved analytically. Our results demonstrate that even symmetric inhomogeneity can affect electric field distribution.

To achieve the best possible therapeutic outcome of the NDBS method, the optimization of stimulation settings to activate a desired region of the brain is essential. To approach this goal in NDBS, we developed two ANNs

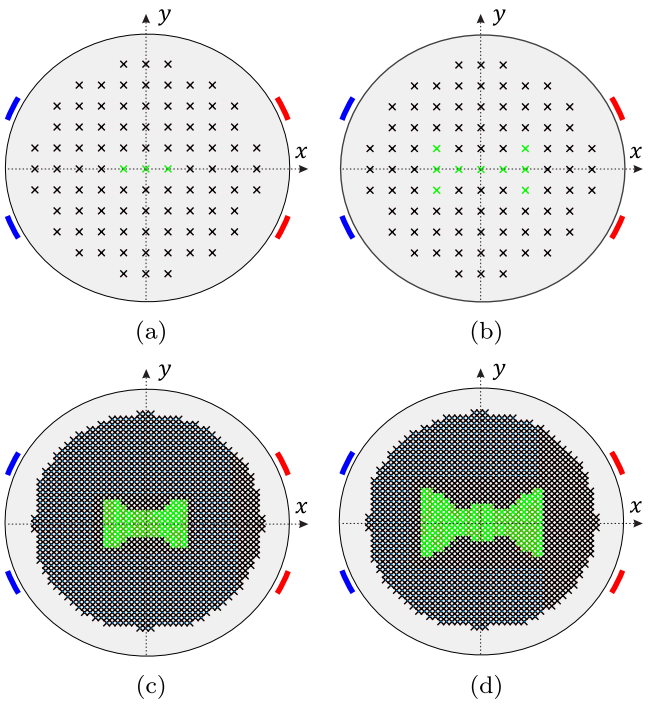


**Figure 8.** (a). The axon model distribution at 4 mm interval in homogeneous model. (b). The axon model distribution at 4 mm interval in inhomogeneous model. (c). The axon model distribution at 1 mm interval in homogeneous model. (d). The axon model distribution at 1 mm interval in inhomogeneous model. Black markers represent the unstimulated axons and green markers represent the stimulated ones. The model is 50 mm diameter infinite cylinder with two electrode pairs which the angle between the center of electrodes and $x$ axis are $-25°$, $25°$, $-155°$, and $155°$ and the arc length of all electrodes is $10°$.

to determine the stimulation parameters based on a desired activated area in IHC with two and four electrode pairs. The results showed the high specificity and sensitivity of two developed ANNs in activating symmetric targets. Also, they demonstrated that there are high correlations between the Euclidean distances of the COG to the contour points in IHC with two electrode pairs and the limitations in controlling the shape of the activated area can be decreased through several methods such as increasing the number of electrode pairs. The results of the developed ANN with four electrode pairs demonstrated this claim. We should mention that the same optimization procedure can be used to develop automatic methods for determining stimulation parameters based on the desired and symmetric activated area location in IIC. In this case, we only need to create new datasets and train ANNs with these new datasets. It may be required to change the number of hidden layers and neurons in them to minimize MSE on the test data. For other ideal models such as homogeneous and inhomogeneous sphere, the procedure is the same. Additionally, it should be noted that we have investigated the possibility of whether ANN could be considered as a possible solution for the problem or not. For this purpose, we have implemented our proposed method for symmetrical electrode placement, and so symmetrical targets. The results suggest that it is a possible solution. If we want to consider non-symmetric targets or targets, not only should we use non-symmetric electrode placements in creating datasets, but also we need more inputs in our ANNs (specify more than one point on the activated area Alzheimer's boundary and calculate their Euclidean distance between the COG and those points). Undoubtedly, for realistic head model incorporating heterogeneity and anisotropy, the optimization problem becomes more challenging. In this case, it is not possible to use fixed electrodes for solving the optimization problem due to asymmetrical features and because the electrodes' positions should be considered as ANN outputs. One possible solution is considering an array of fixed electrodes and different combinations of active electrodes to create a very big dataset; however, results from our other studies using this concept suggest that by choosing the configuration of electrodes appropriately, the activated area is a connected space and thus, we can use the modified version of the proposed optimization algorithm in those models. Finally, it is unmistakably clear that because neither the spatial resolution nor the exact and actual grand truth based on experimental assessments are available for training the ANNs, the proposed ANN may confront multiple limitations in practical uses.

According to Åström *et al* (2015), the excitation electric field thresholds were relatively independent of the stimulation amplitude for different axon size; therefore, we used electric field MEA to determine VTA through the macroscopic approach. The orientation for computing MEA is important and influences the clinical results of stimulation.To the best of our knowledge, determining the most important orientation(s) in the TI stimulation by using *in vitro* and *in vivo* experiments or the exact models considering inhomogeneity and anisotropy

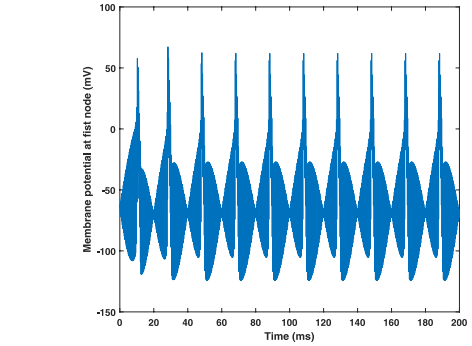


(a)

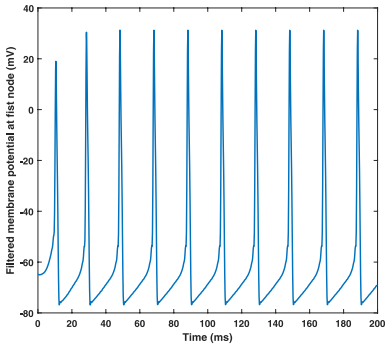


(b)

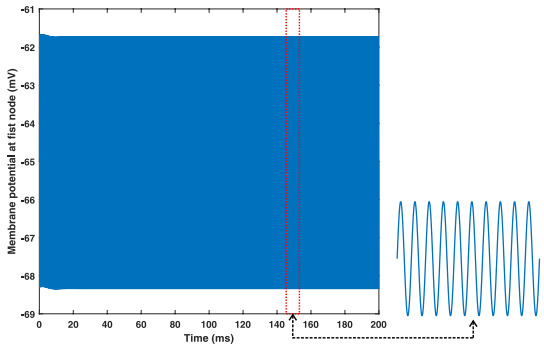


(c)

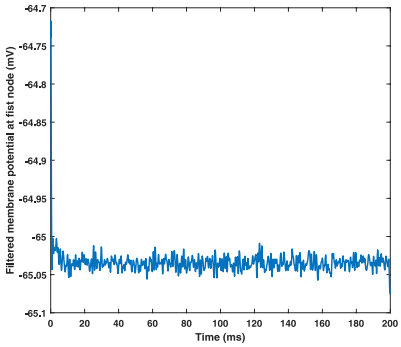


(d)

**Figure 9.** APs in a axon located at the center of the homogeneous model with $I_1 = I_2 = 0.12$ mA and $f_1 = 2500$ Hz at $\phi = 90°$. The geometry is the same as figure 5(c). (a) Membrane potential at first node of axon with $\Delta f = 50$ Hz, (b) Filtered membrane potential at first node of axon with low-pass 10th-order Butterworth filter with 1000 Hz cut off frequency ($\Delta f = 50$ Hz), (c) Membrane potential at first node of axon with $\Delta f = 0$, (d) Filtered membrane potential at first node of axon the model with low-pass 10th-order Butterworth filter with 1000 Hz cut off frequency ($\Delta f = 0$).

was not investigated. Therefore in this paper, we used $|E_{AM}^{max}(x, y)|$ for calculating the activated area to show that in TI stimulation, it is possible to activate deep regions without activating overlaying ones if the configuration of electrodes are chosen appropriately.

The fundamental concept of this new NIBS method is that neurons cannot follow the high frequency components of the input signals due to their low-pass filter behavior. Although this behavior is common among all

**Table 4.** Effect of A. $\Delta f$ and B. $f_1$ on CT in the homogeneous model where the geometry is the same as figure 5(c).

| A | | B | |
|---|---|---|---|
| $\Delta f$ (Hz) | $CT$ ($\mu$A) | $f_1$ (Hz) | $CT$ ($\mu$A) |
| 10 | 293 | 2500 | 94 |
| 20 | 160 | 3000 | 129 |
| 30 | 128 | 3500 | 168 |
| 40 | 105 | 4000 | 210 |
| 50 | 94 | 4500 | 256 |
| 60 | 89 | 5000 | 311 |
| 70 | 96 | 5500 | 387 |
| 80 | 104 | 6000 | 500 |
| 90 | 113 | | |
| 100 | 123 | | |

neurons, the characteristics of this filter are dependent on the neurons' properties. To investigate this fact and also determine the spatial resolution of stimulation, the electrical response of neurons was modeled. The axon Alzheimer's myelin was functioned as a perfect insulator and so, only the membrane dynamics of the nodes of Ranvier reflect the behavior of the model. The AF with the minimum of CT was calculated in homogeneous and inhomogeneous models for four directions and was applied to the axon cable model. Only in $\phi = 90°$ in the middle of the model, APs were generated in the axons (see figure 8). The results of spatial resolution analysis showed that although the activated area was expected to have more length in the $y$ axis compare to the $x$ axis, it did not (see figure 8). By considering more directions, the activated areas may become more similar in macroscopic and microscopic approaches. We should note that the compartmental axon cable model plays an important role in reported results such as CT. More complicated axon cable models were developed in Richardson *et al* (2000) and can be used in future work to investigate the physiological effects of this new NIBS method on the brain tissue more accurately.

The mechanism of high frequency alternating current (HFAC) blocks in neurons was investigated in Pyragas *et al* (2013) and Bhadra *et al* (2007). Based on Bhadra *et al* (2007), there are relationships between the block threshold (defined as the voltage below which the complete block was not obtained), the stimulation frequency and the axon parameters. On the one hand, this phenomenon may be a challenging problem associated with NDBS because it is possible that in some points the amplitude of high frequency electric potential is above the block threshold and the neurons located in these points become blocked, which is undesirable. On the other hand, a specific model for investigating the effect of HFAC on neurons has not been developed yet (to the best of our knowledge) and choosing a model may influence the results. Additionally, the existing experimental data for block phenomenon in frogs (Kilgore and Bhadra 2004), cats (Bhadra *et al* 2006) and rats (Bhadra and Kilgore 2005) are from research on their sciatic nerves, pudendal nerves and peripheral nerves, respectively, and they are not related to the brain Alzheimer's neurons. Future studies are required to investigate how these high frequency electric fields affect the brain.

## 5. Conclusion

In this study, the use of IFC as NDBS was investigated. Computational models were solved analytically, the electric field and potential distributions were calculated based on stimulation parameters and the activated area was determined in the homogeneous and inhomogeneous models. We quantified relationships between stimulation parameters and the location of the activated area. Based on these relationships, two optimization methods for programming NDBS based on ANNs for two and four electrode pairs in the homogeneous models were developed. They offer a possible solution to the challenge of manually adjusting stimulation parameters. The relationship between extracellular electric potential and neural activation to precisely determine the activated area was evaluated. In this study we confronted three main limitations. The first limitation is that we have been forced to use symmetric and simple geometries in which analytical solutions exist. The second limitation is lacking the ground truth data which should be obtained using experimental assessments to train ANNs. Moreover, the developed ANNs can determine the stimulation parameters for activating symmetric targets in the brain. The last limitation is the issue about using electric field MEA to determine VTA through the macroscopic approach that may not be the most important orientation(s) in the TI stimulation. Future work may involve applying this method to a more complex and accurate brain model, increasing the spatial resolution of this method by using arrays of electrode pairs in conjunction with a suitable optimization algorithm. Additionally, deriving activation threshold levels can be used to determine the activated area without requiring compartmental axon cable models.

Moreover, testing this method and proposed optimization algorithms *in vitro* (phantom measurement) and *in vivo* (rat measurement) can be used for further investigating and evaluating its effectiveness for clinical use.

## Acknowledgments

This work has been supported by the Cognitive Sciences and Technologies Council of Iran (CSTC) under Grant No. 6843.

## ORCID iDs

Ahmadreza Attarpour https://orcid.org/0000-0001-5890-5740
Rassoul Amirfattahi https://orcid.org/0000-0002-7917-1683

## References

Agharezaee M and Mahnam A 2015 A computational study to evaluate the activation pattern of nerve fibers in response to interferential currents stimulation *Med. Biol. Eng. Comput.* **53** 713–20
Anderson D N, Osting B, Vorwerk J, Dorval A D and Butson C R 2018 Optimized programming algorithm for cylindrical and directional deep brain stimulation electrodes *J. Neural Eng.* **15** 026005
Åström M, Diczfalusy E, Martens H and Wårdell K 2015 Relationship between neural activation and electric field distribution during deep brain stimulation *IEEE Trans. Biomed. Eng.* **62** 664–72
Åström M, Lemaire J J and Wårdell K 2012 Influence of heterogeneous and anisotropic tissue conductivity on electric field distribution in deep brain stimulation *Med. Biol. Eng. Comput.* **50** 23–32
Balanis C A 1999 *Advanced Engineering Electromagnetics* (New York: Wiley)
Bhadra N and Kilgore K L 2005 High-frequency electrical conduction block of mammalian peripheral motor nerve *Muscle Nerve* **32** 782–90
Bhadra N, Bhadra N, Kilgore K and Gustafson K J 2006 High frequency electrical conduction block of the pudendal nerve *J. Neural Eng.* **3** 180
Bhadra N, Lahowetz E A, Foldes S T and Kilgore K L 2007 Simulation of high-frequency sinusoidal electrical block of mammalian myelinated axons *J. Comput. Neurosci.* **22** 313–26
Butson C R and McIntyre C C 2008 Current steering to control the volume of tissue activated during deep brain stimulation *Brain Stimul.* **1** 7–15
Chaturvedi A, Butson C R, Lempka S F, Cooper S E and McIntyre C C 2010 Patient-specific models of deep brain stimulation: influence of field model complexity on neural activation predictions *Brain Stimul.* **3** 65–77
Chaturvedi A, Luján J L and McIntyre C C 2013 Artificial neural network based characterization of the volume of tissue activated during deep brain stimulation *J. Neural Eng.* **10** 056023
Cheng D K *et al* 1989 *Field and Wave Electromagnetics* (Boston, MA: Addison-Wesley)
Cubo R, Åström M and Medvedev A 2016 Optimization of lead design and electrode configuration in deep brain stimulation *Int. J. Adv. Life Sci.* **8** 76–86
Cubo R, Åström M and Medvedev A 2018 Optimization-based contact fault alleviation in deep brain stimulation leads *IEEE Trans. Neural Syst. Rehabil. Eng.* **26** 69–76
Dayan E, Censor N, Buch E R, Sandrini M and Cohen L G 2013 Noninvasive brain stimulation: from physiology to network dynamics and back *Nat. Neurosci.* **16** 838
Fox M D, Buckner R L, Liu H, Chakravarty M M, Lozano A M and Pascual-Leone A 2014 Resting-state networks link invasive and noninvasive brain stimulation across diverse psychiatric and neurological diseases *Proc. Natl Acad. Sci.* **111** E4367–75
Gmel G E, Hamilton T J, Obradovic M, Gorman R B, Single P S, Chenery H J, Coyne T, Silburn P A and Parker J L 2015 A new biomarker for subthalamic deep brain stimulation for patients with advanced Parkinson's disease – a pilot study *J. Neural Eng.* **12** 066013
Goats G 1990 Interferential current therapy *Br. J. Sports Med.* **24** 87
Grossman N *et al* 2017 Noninvasive deep brain stimulation via temporally interfering electric fields *Cell* **169** 1029–41
Gunalan K, Chaturvedi A, Howell B, Duchin Y, Lempka S F, Patriat R, Sapiro G, Harel N and McIntyre C C 2017 Creating and parameterizing patient-specific deep brain stimulation pathway-activation models using the hyperdirect pathway as an example *PLoS One* **12** e0176132
Hodgkin A L and Huxley A F 1952 A quantitative description of membrane current and its application to conduction and excitation in nerve *J. Physiol.* **117** 500–44
Howell B and McIntyre C C 2016 Analyzing the tradeoff between electrical complexity and accuracy in patient-specific computational models of deep brain stimulation *J. Neural Eng.* **13** 036023
Hutcheon B and Yarom Y 2000 Resonance, oscillation and the intrinsic frequency preferences of neurons *Trends Neurosci.* **23** 216–22
Kilgore K L and Bhadra N 2004 Nerve conduction block utilising high-frequency alternating current *Med. Biol. Eng. Comput.* **42** 394–406
Kringelbach M L, Jenkinson N, Owen S L and Aziz T Z 2007 Translational principles of deep brain stimulation *Nat. Rev. Neurol.* **8** 623
Marquardt D W 1963 An algorithm for least-squares estimation of nonlinear parameters *J. Soc. Ind. Appl. Math.* **11** 431–41
McIntyre C C, Richardson A G and Grill W M 2002 Modeling the excitability of mammalian nerve fibers: influence of afterpotentials on the recovery cycle *J. Neurophysiol.* **87** 995–1006
Miocinovic S, Lempka S F, Russo G S, Maks C B, Butson C R, Sakaie K E, Vitek J L and McIntyre C C 2009 Experimental and theoretical characterization of the voltage distribution generated by deep brain stimulation *Exp. Neurol.* **216** 166–76
Nitsche M A *et al* 2008 Transcranial direct current stimulation: state of the art 2008 *Brain Stimul.* **1** 206–23
Oluigbo C O, Salma A and Rezai A R 2012 Deep brain stimulation for neurological disorders *IEEE Rev. Biomed. Eng.* **5** 88–99
Peña E, Zhang S, Deyo S, Xiao Y and Johnson M D 2017 Particle swarm optimization for programming deep brain stimulation arrays *J. Neural Eng.* **14** 016014
Pinsky M A 2008 *Introduction to Fourier Analysis and Wavelets* vol 102 (Providence, RI: American Mathematical Society)

Polanía R, Nitsche M A and Ruff C C 2018 Studying and modifying brain function with non-invasive brain stimulation *Nat. Neurosci.* **21** 174–87

Pyragas K, Novičenko V and Tass P A 2013 Mechanism of suppression of sustained neuronal spiking under high-frequency stimulation *Biol. Cybern.* **107** 669–84

Raspopovic S, Capogrosso M and Micera S 2011 A computational model for the stimulation of rat sciatic nerve using a transverse intrafascicular multichannel electrode *IEEE Trans. Neural Syst. Rehabil. Eng.* **19** 333–44

Rattay F 1986 Analysis of models for external stimulation of axons *IEEE Trans. Biomed. Eng.* **BME-33** 974–7

Richardson A, McIntyre C and Grill W 2000 Modelling the effects of electric fields on nerve fibres: influence of the myelin sheath *Med. Biol. Eng. Comput.* **38** 438–46

Roth Y, Zangen A and Hallett M 2002 A coil design for transcranial magnetic stimulation of deep brain regions *J. Clin. Neurophysiol.* **19** 361–70

Walckiers G 2009 Bio-electromagnetic model of deep brain stimulation *PhD thesis* EPFL University (https://doi.org/10.5075/epfl-thesis-4369)

Ward A R 2016 Electrical stimulation using kilohertz-frequency alternating current *Phys. Ther.* **89** 181–90